Chapter-4

Soft Chemical Synthesis and Visible-Light Photocatalytic Activities of α-$AgVO_3$ Nanorods and $BiVO_4$ Nanobars

✶ **A part of this work has been accepted for publication:**

T. George, S. Joseph, A. T. Sunny, S. Mathew, *Int. J. Nanotechnology*, (2009) (in press)

✶ **A part of this work has been presented :**

1. T.George, S. Joseph, S. Mathew, *National Seminar on Frontiers in Chemistry 2006*, FIC-06, Department of Applied Chemistry, CUSAT, Kerala, 24-25 March, 2006

2. T. George, S. Joseph, A. T. Sunny, S. Mathew, *International Conference, NAG-2007,* JNCASR, Bangalore, 21-23 January, 2007

3. T. George, S. Joseph, A. T. Sunny, S. Mathew, *International Conference on Advanced Materials,* ICAM-2008, SCS, M.G. University, Kerala, 18-21 February, 2008

4.1 Introduction

Tuning the size and dimensionality of nanostructures is one of the most challenging issues faced by researchers. One-dimensional nanostructures have been called by a variety of names including whiskers, fibers, nanowires and nanorods. Nanorods with high aspect ratio have generated considerable interest globally due to their potential applications in the next generation of nano and molecular electronics. The synthesis of nanomaterials with controlled sizes and shapes is critical to these applications since shapes influence electronic properties. Researchers are interested in the synthesis of semiconducting nanocrystals with desired size, morphology and crystal structure which can be grown efficiently in different forms such as nanoparticles, nanorods, nanobars and nanowires. These semiconductors with varying morphology have attracted much attention due to their novel properties and promising applications [1-3].

Many techniques like template-based electroplating, solution-liquid-solid growth (SLS) and spontaneous anisotropic growth have been developed in the synthesis and formation of one-dimensional nanostructured materials. Colloidal precipitation is an effective bottom-up approach in the synthesis of nanoparticles with precise control over shape and size [4]. The kinetics of nucleation and particle growth in homogeneous solutions can be adjusted by the controlled release of the anions and cations. Careful control of the kinetics of the precipitation can result in monodisperse nanoparticles. The particle size is influenced by the reactant concentration, pH and temperature [5]. Many groups have reported the kinetically controlled growth of rod-like morphologies [6-14].

In this chapter we describe the kinetically controlled growth of $AgVO_3$ nanorods and $BiVO_4$ nanobars by a colloidal precipitation method. To the best of our knowledge, room temperature synthesis of monoclinic α-$AgVO_3$ and monoclinic $BiVO_4$ nanobars have not been reported till date. Monoclinic α-$AgVO_3$ nanorods (thickness 30 nm) and monoclinic $BiVO_4$ nanobars (thickness 15 nm) with high aspect ratio are prepared by controlling the reaction kinetics of precipitation at room temperature, without using any capping agents or surfactants. The nanocrystalline vanadates are characterized using XRD, SEM, EDAX, FE-SEM, TEM and AFM. Possible growth mechanisms of the nanocrystals are explained by the oriented attachment of flocs through an anisotropic growth. Ag nanoparticles are formed *in-situ* on $AgVO_3$ nanorods. Using diffuse reflectance spectral analysis the band gap of α-$AgVO_3$ nanorods and $BiVO_4$ nanobars are calculated and their photocatalytic behavior is investigated by photodegradation of methylene blue. The α-$AgVO_3$ nanorods have higher pore volume compared to $BiVO_4$ nanobars. The Ag nanoparticles attached on the surface of $AgVO_3$ nanorods serve as active sites for photocatalysis. Hence silver vanadate nanorods exhibit enhanced photocatalytic activity compared to $BiVO_4$ nanobars and is a good candidate for visible light driven photocatalysis. Selective synthesis of tetragonal and monoclinic $BiVO_4$ powders by aqueous processes has been reported recently [15].

Photocatalysis has been established as an efficient and promising technology for the removal of toxic organic and inorganic contaminates from water [16]. Some metal oxide semiconductors like titanium dioxide, zinc oxide, tungsten oxide, strontium titanate, and hematite are proven to be dynamic photocatalysts [17]. Most of these semiconductor photocatalysts have

band gap in the ultraviolet (UV) region, *i.e.*, equivalent to or larger than 3.2 eV (λ = 387 nm). Therefore, they promote photocatalysis upon illumination with UV radiation. Unfortunately solar spectrum consists only 5–7% of UV light, while 46% and 47% of the spectrum has visible light and infrared radiation, respectively [18]. Use of ultra violet light in bulk level, for the treatment of huge quantity of industrial effluents is not much feasible and economical. However, photocatalytic degradation of organic contaminants using solar irradiation could be highly economical compared with the processes using artificial UV irradiation, which required substantial electrical power input. Therefore, improving photocatalytic activity by modification has become a hot topic among researchers in recent years [19, 20].

In the countries where ample amount of sunlight is available, photo catalysis involving sunlight will be economical and preferable. Therefore, there is a need of effective photo catalyst which undergoes photo catalytic degradation of organic pollutants under sunlight or visible light irradiation and the development of visible-light driven photocatalysts has become one of the most challenging topics today. In this situation, photocatalytic properties of quite a few metal oxides different from TiO_2, WO_3 and ZnO have been explored to overcome this difficulty. As a result, it was found that some vanadates show good photocatalytic activities in visible range [21, 22]. In recent years, vanadium oxides and their combinations have been the subject of numerous investigations because of its wide ranging applications in catalysis and material science [23, 24].

The band gap energies of vnadates are lower than other photocatalysts like TiO_2 or WO_3. The diffuse reflection spectral analysis shows that silver vanadate has a low band gap of about 2.4 eV and is a candidate for UV-visible light driven photocatalysts [25]. Monoclinic bismuth vanadate with band gap

2.3 eV, is an effective photocatalyst for water splitting and pollutant photodegradation under visible-light irradiation and has attracted increasing attention recently [26-28]. The present study focuses on the efficient use of sunlight and the ability of α-$AgVO_3$ nanorods and $BiVO_4$ nanobars to photo catalytic degradation of organic pollutants under sunlight or visible light irradiation.

4.2. Synthesis and characterization of α-$AgVO_3$ nanorods

All the chemicals for the synthesis were purchased from Sigma Aldrich Chemicals (purity 99.9%) and used without further purification. Equimolar aqueous solutions (0.003M) of analar silver nitrate ($AgNO_3$) and ammonium metavanadate (NH_4VO_3) were mixed at room temperature, along with vigorous stirring. The precipitate formed was filtered, washed and dried at room temperature. The product was identified by Bruker D8 Advance X-ray diffractometer using Cu K_α radiation (λ = 1.5406 Å). The morphology of the silver vanadate nanostructures was examined with scanning electron microscope (JEOL-JSM- 5600 LV) at 20 kV accelerating voltage. The chemical compositions of the samples were analyzed by Oxford INCA energy dispersive X-ray analysis (EDAX) system. The powder sample was put on a carbon coated copper grid and air blown for uniform coating, and then sputtered with gold in argon atmosphere. The atomic force microscopic (AFM) image was taken by tapping mode using a multimode atomic force microscope (Nanoscope IV controller). The powder sample was ultrasonicated in ethanol for 5-10 minutes and then by drop-casting method, placed on a mica surface of 4mm x 5mm surface area. After drying it was struck to the sample holder.

The size and morphology of the α-$AgVO_3$ nanorods were determined by transmission electron microscope (TEM), TECNAI F30 FEG model instrument operated at an accelerating voltage of 300 kV. The sample was ultrasonically dispersed in ethanol for several minutes prior to depositing on to the copper grid and the solvent was evaporated. The specific surface area of α-$AgVO_3$ nanorods were determined by the BET (Brunauer, Emmett and Teller) method with nitrogen adsorption using Gemini Micromeritics surface area and porosity analyzer at 77 K, after degassing the sample in a flow of N_2 at 180°C for 5 hours. The BET surface area was calculated from the linear part of the BET plot (P/P_0 = 0.1–0.25). The UV–vis diffuse reflectance spectra of α-$AgVO_3$ nanorods were measured by a UV–vis spectrometer (Shimadzu UV-2550) using $BaSO_4$ as a reference, and were converted from reflection to absorbance by the Kubelka–Munk method [29].

4.3. Synthesis and characterization of $BiVO_4$ nanobars

The synthesis of monoclinic $BiVO_4$ nanobars was as follows. 0.5 g analar bismuth nitrate (Bi $(NO_3)_3.5H_2O$) purchased from Sigma Aldrich Chemicals (purity 99.9%) was dissolved in 100 ml distilled water with stirring. The bismuth nitrate is sparingly soluble in water due to the formation of bismuth oxy-nitrate. The clear solution was decanted and mixed with 100 ml, 0.01M aqueous solution of analar ammonium metavanadate (Sigma Aldrich, purity 99.9%), along with vigorous stirring at room temperature. The precipitate formed was filtered, washed and dried at room temperature.

The product was identified by PANalytical X'Pert PRO Multipurpose diffractometer using Cu K_α radiation (λ = 1.5406 Å). Studies on the surface morphology, homogeneity and energy-dispersive X-ray analysis (EDAX) of

the powders were carried out using a field emission scanning electron microscope (NOVA NANOSEM 600 FEI).

The specific surface area of $BiVO_4$ nanobars were determined by the BET (Brunauer, Emmett and Teller) method with nitrogen adsorption using Gemini Micromeritics surface area and porosity analyzer at 77 K, after degassing the samples in a flow of N_2 at 180°C for 5 hours. The BET surface area was calculated from the linear part of the BET plot (P/P_0 = 0.1–0.25). Optical absorption spectra of $BiVO_4$ nanobars were measured by a UV–vis spectrometer (Shimadzu UV-2550) using $BaSO_4$ as a reference and were converted from reflection to absorbance by the Kubelka–Munk method [29].

4.4. Photocatalytic study of α-$AgVO_3$ nanorods and $BiVO_4$ nanobars

To study the photocatalytic activities of α-$AgVO_3$ nanorods and $BiVO_4$ nanobars, the dye methylene blue (MB) with a major absorption band at 665 nm was chosen as a model pollutant. 0.1g of α-$AgVO_3$/$BiVO_4$ was added to 250 ml of an aqueous solution of ($2x10^{-5}$ mol dm^{-3}) MB solution with vigorous stirring. The resulting mixture was kept in the dark for 30 minutes to maximize the adsorption of the dye on the surface of α-$AgVO_3$/$BiVO_4$. The MB solution was then collected by centrifugation and the absorption maximum corresponding to the concentration of MB at zero time of irradiation of light, C_o was measured by UV-visible spectroscopy. The MB solution containing α-$AgVO_3$/$BiVO_4$ was stirred at intervals. The suspension was collected by centrifugation and absorption was measured at 15 minutes exposure time intervals for 3 hours to get the values of C_t (absorption maximum at time interval, t). Then C_t/C_o was plotted against illumination

time. The experiment was repeated for the direct photolysis of MB in the absence of the catalysts, and the results were compared.

4.5. Results and discussion

4.5.1. XRD study of α-$AgVO_3$ nanorods

The X-ray powder diffraction pattern for silver vanadate is shown in figure 4.1. All the diffraction peaks in the patterns are indexed based on the JCPDS file [30] of α-$AgVO_3$ with space group $I_{2/}m$.

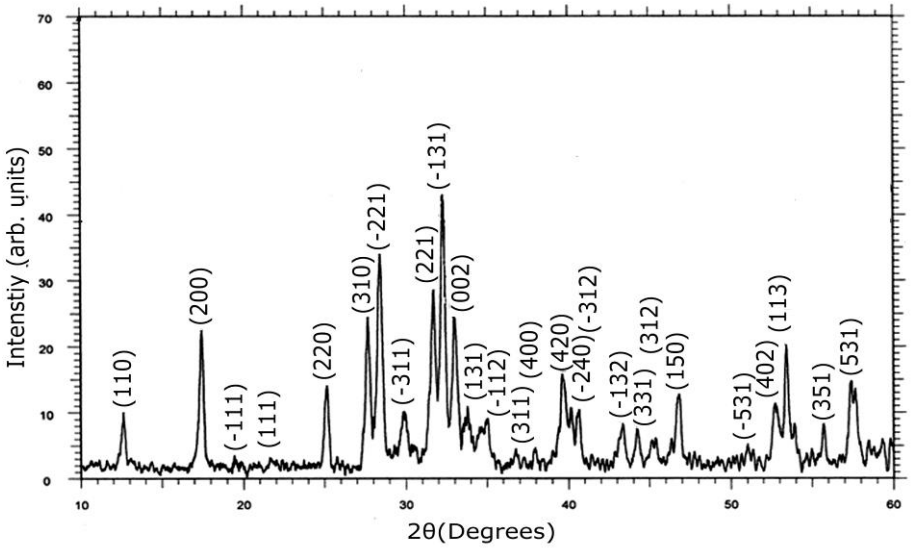

Figure 4. 1. X-ray powder diffraction pattern for silver vanadate nanorods

The diffraction pattern reveals the phase purity and the crystalline nature of the sample belong to the monoclinic system. The unit cell parameters calculated using 'Fullprof' program are a = 10.432 Å, b = 9.891 Å and c = 5.525 Å. These results are consistent with the JCPDS data of α-$AgVO_3$

viz, a = 10.437 Å, b = 9.897 Å and c = 5.532 Å with α = γ = 90°, β = 99.69°. The average crystallite size calculated using the Scherrer formula is 30 nm.

4.5.2. XRD study of $BiVO_4$ nanobars

Figure 4.2 shows the X-ray powder diffraction pattern for bismuth vanadate nanobars. A trace amount of a tetragonal phase can also be seen whose peaks are marked by dots.

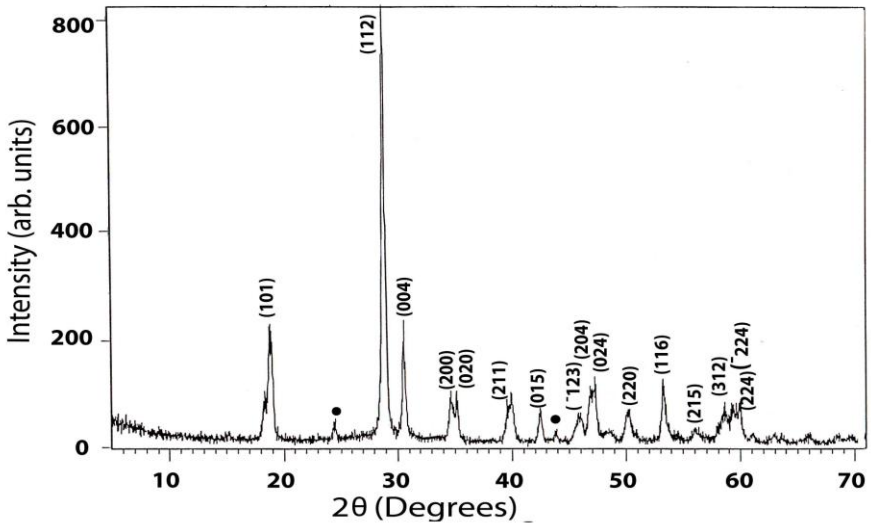

Figure 4.2. X-ray powder diffraction pattern for bismuth vanadate nanobars

All the remaining peaks in the patterns are indexed on the basis of the crystallographic data of the known structures of monoclinic $BiVO_4$ [31] with space group $I_{2/b}$. The crystallinity of the BiVO4 nanobars belonging to the monoclinic system is well evident from the XRD pattern. The unit cell parameters calculated using 'Fullprof' program and are a = 5.196, b = 5.091 Å, c = 11.694 Å. These results are consistent with the JCPDS data of $BiVO_4$ *viz,* a = 5.193 Å, b = 5.089 Å, c =11.69 Å and α = γ = 90°,

β = 90.387°). The average crystallite size of the $BiVO_4$ nanobars calculated from the line broadening of the XRD peaks using Scherrer formula is 15 nm.

4.5.3. Scanning electron microscopic study of α-$AgVO_3$ nanorods

The SEM images in figure 4.3 (a,b) indicate that the α-$AgVO_3$ crystals have rod-like morphologies. The energy dispersive X-ray analysis spectrum

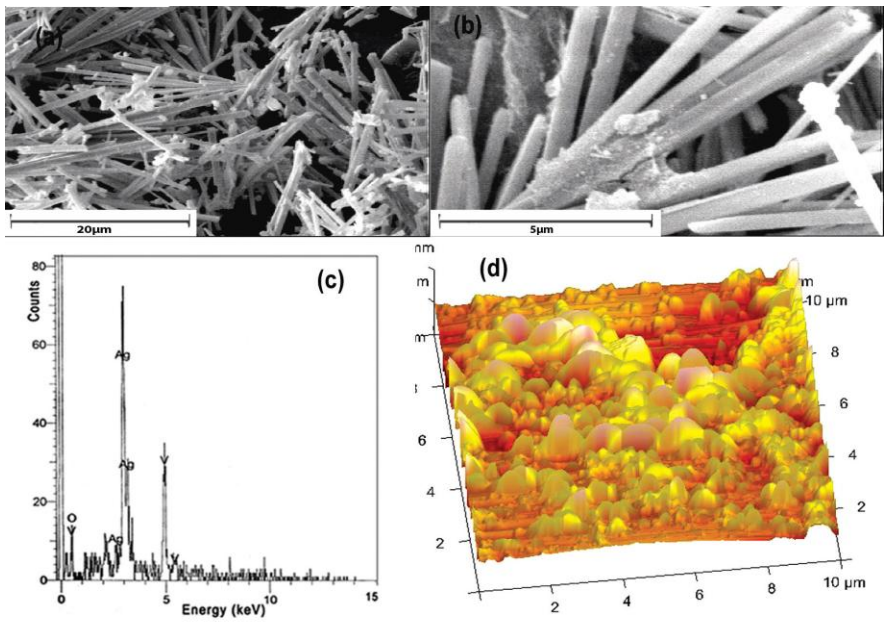

Figure 4.3 (a, b) SEM images of α-$AgVO_3$ nanorods **(c)** EDS of α-$AgVO_3$ nanorods **(d)** AFM image of α-$AgVO_3$ nanorods

(EDS) shown in figure 4.3 (c) shows the co-existence of silver, vanadium and oxygen in the synthesized sample. The AFM image in figure 4.3 (d) also reveals the rod-like nature of the crystals.

4.5.4. Transmission electron microscopic study of α-$AgVO_3$ nanorods

The TEM images in figure 4.4 (a, b, c, d) reveal that the silver vanadate nanorods are decorated with silver metal particles. Such reduced

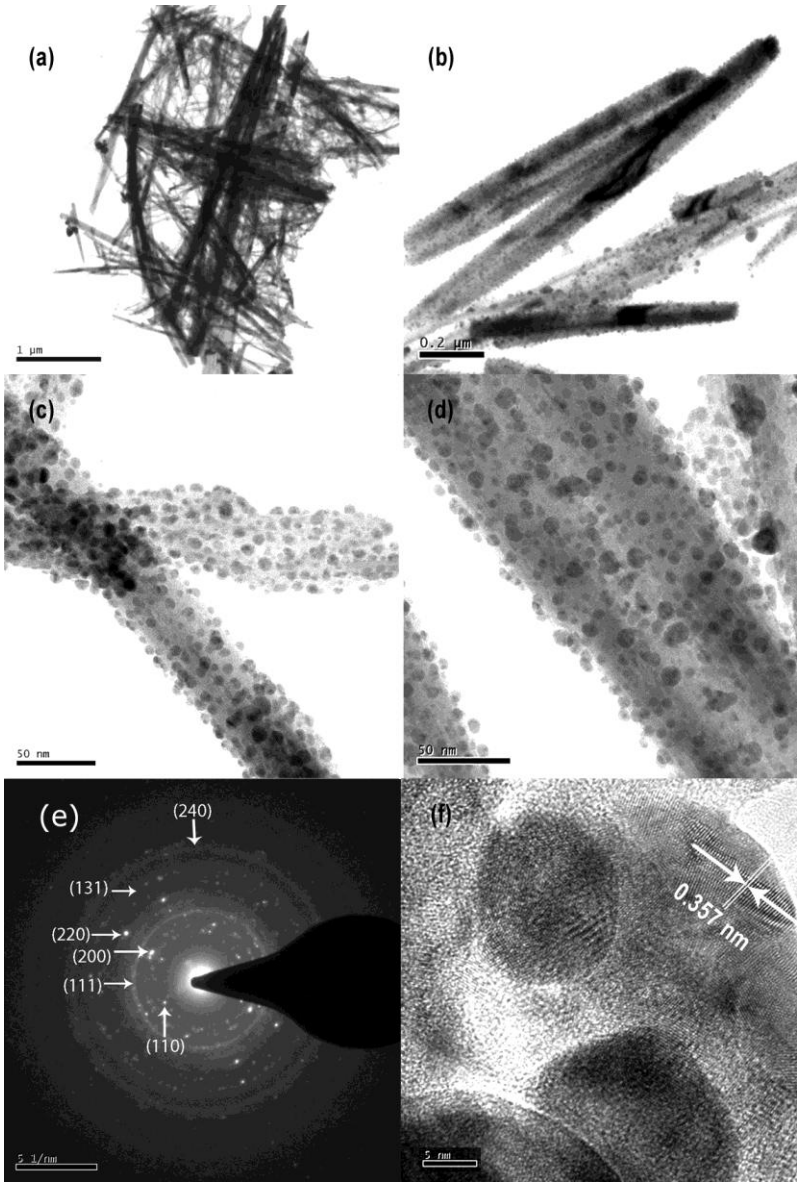

Figure 4.4 (a) TEM images of a typical α-$AgVO_3$ nanorod bundle **(b, c, d)** the TEM images of the decorated nanorods **(e)** the SAED pattern of the nanorods **(f)** HRTEM image of a nanorod lattice

silver metal particles have been reported on silver vanadate nanorods by ion exchange synthesis [32]. In the reaction, $AgNO_3$ plays dual roles in the formation of $Ag/AgVO_3$ nanocomposites. $AgNO_3$ react with NH_4VO_3 to form $AgVO_3$ nanorods. Also Ag nanoparticles are formed by the reduction of $AgNO_3$ in solution resulting in the formation of $Ag/AgVO_3$ nanocomposites. The molar concentration of $AgNO_3$ play an important role in the self reduction and substitution reactions of $AgNO_3$ to form Ag nanoparticles supported on $AgVO_3$ nanorods. It is supposed that the formation of $Ag/AgVO_3$ nanocomposites is related to the good affinity between them. Literature reports reveal that Ag+ ion in the $AgVO_3$ lattice serve as the nucleation sites for the deposition of Ag nanoparticles on the surfaces of $AgVO_3$ nanorods [33].

The particle size estimated from TEM result is consistent with the XRD result. Typical high magnification images in figure 4.4 (c, d) shows that the nanorods are highly porous. The selected area electron diffraction (SAED) pattern (figure 4.4 (e)) reveals the polycrystalline nature of the synthesized nanorods and the rings are indexed as (110), (200), (111), (220), (131) and (240) reflections of the monoclinic α-$AgVO_3$. The TEM observations show that the length of the nanorods ranges from 2-3 μm with diameter, 30 nm indicting large aspect ratio. The HRTEM image (figure 4.4 (f)) taken from the nanorod clearly shows the crystalline lattice decorated with Ag particles. The Ag nanoparticles dispersed on the $AgVO_3$ substrate are very sparse and with diameters of about 5–10 nm. The interplanar distance is about 3.57 Å, which corresponds to the (220) lattice spacing of α-$AgVO_3$ and is consistent with the XRD results.

The surface area calculated by BET method for α-$AgVO_3$ nanorods is 17.16 m^2/g and the pore volumes is 0.03 x 10^{-6} m^3/g.

4.5.5. Field emission electron microscopic study of $BiVO_4$

The FESEM image in figure 4.5 shows the bar-like morphology of the $BiVO_4$ nanoparticles. The thickness of each bar is estimated to be 15 nm. Each bar is having a length of several micrometers. Hence they have high aspect ratio.

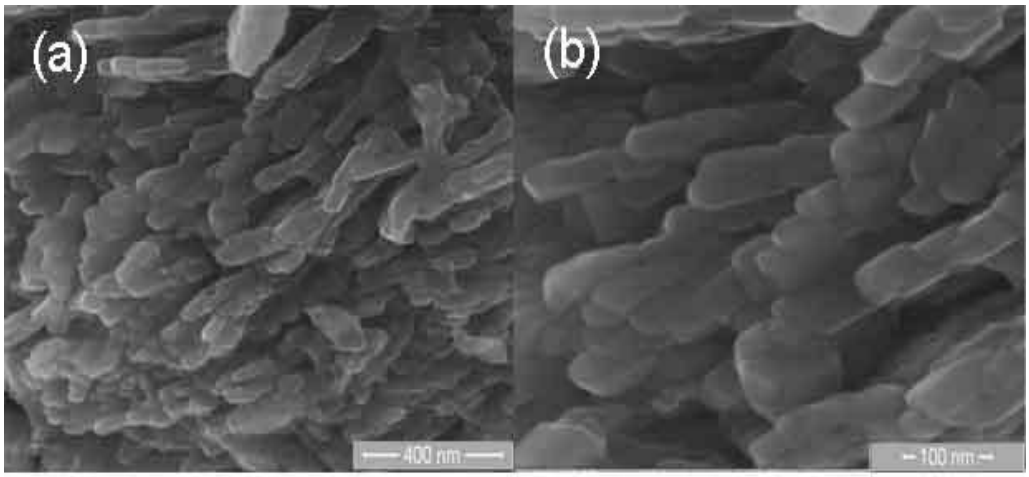

Figure 4.5. FESEM images of $BiVO_4$ nanobars

The EDAX report shown in figure 4.6 reveals the purity and the co-existence of Bismuth, Vanadium and Oxygen in stoichiometric ratios in the synthesized $BiVO_4$ nanobars.

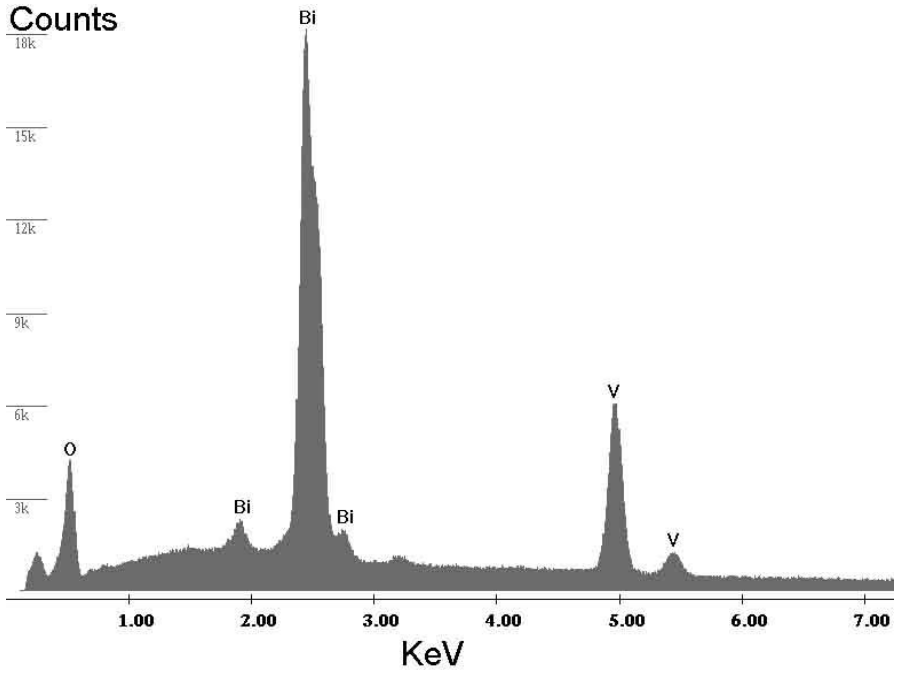

Figure 4. 6. EDS of bismuth vanadate nanobars

The surface area calculated by BET method for $BiVO_4$ nanobars is 17.34 m^2/g and the estimated pore volume is 0.02 $x10^{-6}$ m^3/g.

4.5.6. Growth mechanism of α-$AgVO_3$ nanorods and $BiVO_4$ nanobars

The formation of silver vanadate nanorods and bismuth vanadate nanobars can be explained by the oriented attachment of flocs through an anisotropic growth. Schematic diagram for the formation of nanorods and nanobars from aqueous solutions of the precursors are shown in figure 4.7.

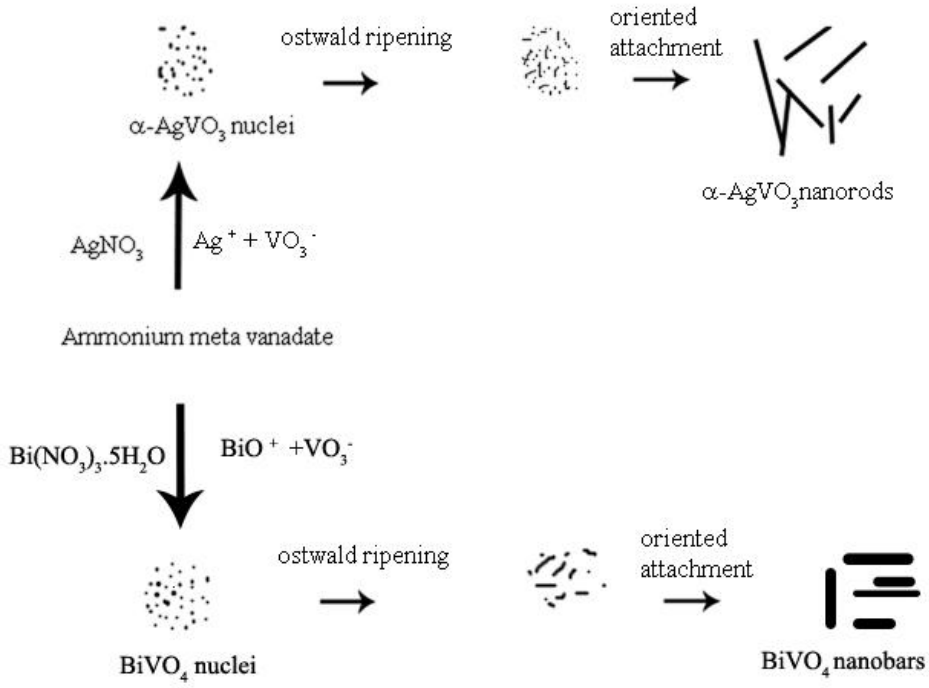

Figure 4.7. Schematic growth diagram of nanorods and nanobars

The positive ions and the negative ions are under the influence of Brownian motion in solution. Coagulation, which occurs under the influence of Brownian motion, is called perikinetic coagulation. However the rate of particle collision and the rate of coagulation can be enhanced by the hydrodynamic forces created by rapid stirring.

When the nuclei are sufficiently small, the available thermal energy causes their structure to fluctuate, allowing defects to form or be removed depending upon their energetic favorability [34]. Most of the nuclei formed incorporate boundary defects because such defects enable a lower surface energy [35]. As nuclei grow, changes in the defect structure become too

costly, relative to the available thermal energy and they become stuck in a given morphology. The morphology of flocs is determined to a large extent by the nature of the interparticle forces involved [36]. Thus, if the particles are strongly repelling but sediment under gravity, they tend to form a close-packed structure because the particles can slide across one another under the influence of Brownian motion and seek out a configuration of minimum energy [37]. Here the charge carriers under the influence of hydrodynamic forces can move in one dimension and occupy quantized states in the other two dimensions. By aggregation, the particles might connect in to a linear shape and then by experiencing an Ostwald ripening process; the linear-like aggregates recrystallize into perfect 1D structure along the preferred orientation.

4.5.7. Optical studies of α-$AgVO_3$ nanorods and $BiVO_4$ nanobars

The UV–visible diffuse reflectance spectra of the as-prepared monoclinic α-$AgVO_3$ nanorods and $BiVO_4$ nanobars are shown in figure 4.8 (a) and 4.9 (a). The steep shape of the spectra indicates that the visible light absorption is not due to the transition from the impurity level but due to the band-gap transition [38]. It is found that the absorption edges of the monoclinic α-$AgVO_3$ and the monoclinic $BiVO_4$ are quite different. The absorption edge of α-$AgVO_3$ prepared at room temperature starts at about 500 nm while it extends to 555 nm for monoclinic $BiVO_4$ nanobars prepared at the same temperature.

In α-$AgVO_3$ the valence band is composed of Ag 4d and O 2p orbitals. The characteristic absorption band observed for monoclinic α-$AgVO_3$ is due to the transition of electrons from the Ag 4d and O 2p valence band orbitals to empty 3d conduction band of V^{5+} [39].

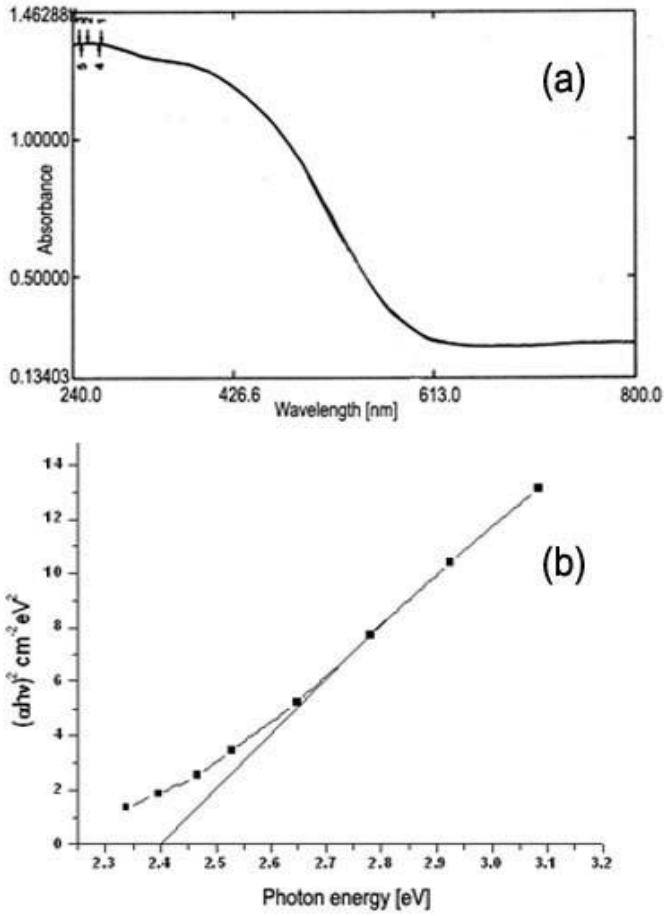

Figure 4.8 (a) UV- visible diffuse reflectance spectrum **(b)** Plot of (hν) against $(\alpha h\nu)^2$ of α-$AgVO_3$ nanorods

The absorption band in monoclinic $BiVO_4$ is assigned to the transition of electrons from 6s valence band of Bi^{3+} to empty 3d conduction band orbitals of V^{5+} [40]. As a crystalline semiconductor, the optical absorption near the band edge follows the formula $\alpha h\nu = A(h\nu - Eg)^{n/2}$ [41] , where α, ν, Eg and A are absorption coefficient, light frequency, band gap and a constant respectively.

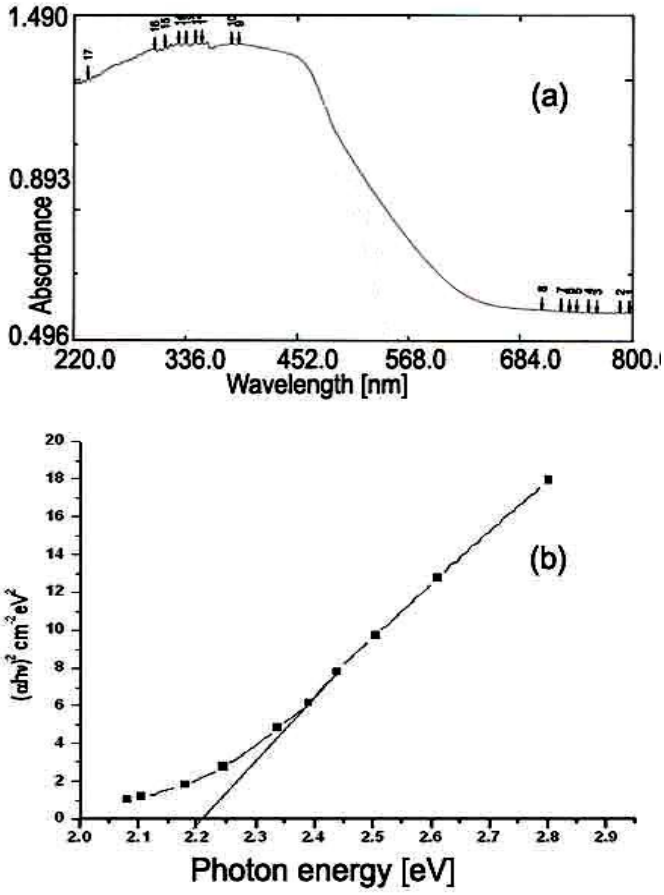

Figure 4.9 (a) UV- visible diffuse reflectance spectrum **(b)** Plot of (hν) against $(\alpha h\nu)^2$ of $BiVO_4$ nanobars

Among them, n depends on the characteristics of the transition in a semiconductor, *i.e.* direct transition (n = 1) or indirect transition (n = 4). From literature reports, for $AgVO_3$ and $BiVO_4$, n = 1 [41, 42]. The band gap energy (Eg value) can be estimated from a plot $(\alpha h\nu)^2$ *versus* photon energy (hν). The intercept of the tangent to the X-axis will give a good approximation of the band gap energy for the photocatalyst [40-45]. Plots of the $(\alpha h\nu)^2$ versus

photon energy (hv) of α-$AgVO_3$ nanorods and $BiVO_4$ nanobars are shown in figure 4.8 (b) and figure 4.9 (b). The band gap energies are calculated as 2.40 eV for α-$AgVO_3$ and 2.22 eV for $BiVO_4$.

4.5.8. Photocatalytic properties

Figure 4.10 (a) shows the plots of C_t/C_o against illumination time and figure 4.10 (b) shows the plots of efficiency against illumination time for the direct photolysis of MB and the photocatalytic degradation of MB in presence of the catalysts.

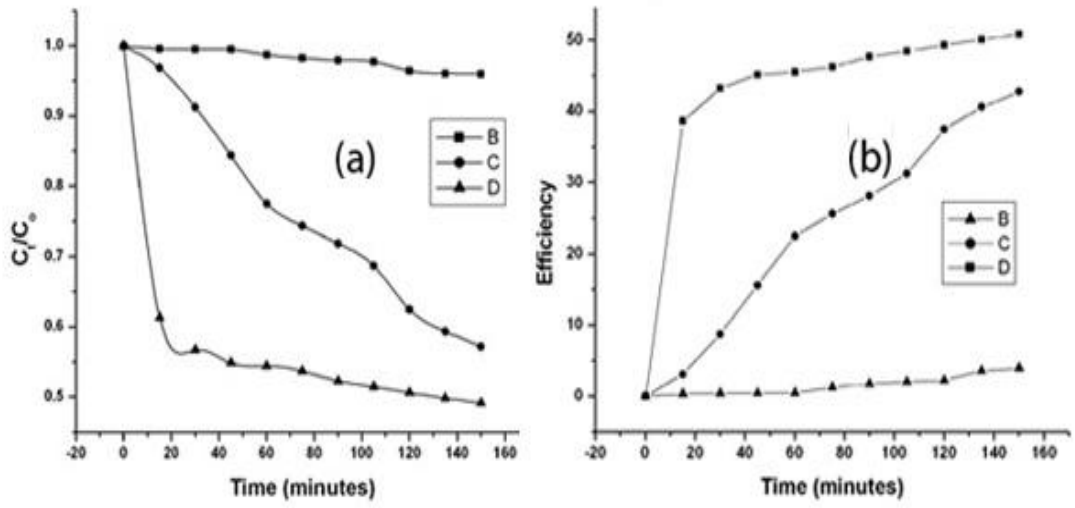

Figure 4.10 (a) Plots of C_t/C_o against time **(b)** efficiency against time for the photocatalytic degradation of methylene blue **(B)** in the absence of the catalysts **(C)** in the presence of $BiVO_4$ and **(D)** in the presence of α-$AgVO_3$

MB is commonly used as a representative of widespread organic dyes, that contaminate textile effluents and that are very difficult to decompose in

waste streams under visible-light irradiation. MB shows a major absorption wavelength at 665 nm. From figure 4.10 (a), it is quite evident that the extent of self photodegradation of MB is very small compared to its photocatalytic degradation in presence of sliver vanadate and bismuth vanadate. The curve (B) corresponds to MB dissolved in water and exposed to visible light, which shows a slight degradation, because of OH^- in water. The curve (C) shows the photodegradation of MB in presence of $BiVO_4$ nanobars. The curve (D) corresponds to the degradation of the dye in presence of α-$AgVO_3$ nanorods. The photocatalytic efficiencies are calculated using the relation [46],

$$\eta = \frac{(C_0 - C_t) \times 100}{C_0}$$

where η is the percentage photocatalytic efficiency, C_0 is the initial concentration of reactant and C_t is the concentration of the reactant after illumination time t. The photocatalytic efficiencies of α-$AgVO_3$ nanorods and $BiVO_4$ nanobars calculated after 150 minutes of visible light irradiation is 51% and 43% respectively, and the self degradation efficiency of MB within this time is found to be only below 4% as shown in figure 4.10 (b). However, about 45% of the MB is degraded within 30 minutes by α-$AgVO_3$ nanorods. At this time the degradation efficiency of $BiVO_4$ nanobars is only 10% and the self degradation efficiency of MB is 0%.

The calculated band gap, 2.22 eV of $BiVO_4$ nanobars is smaller than that 2.40eV, of α-$AgVO_3$ nanorods. But α-$AgVO_3$ nanorods are more efficient compared to $BiVO_4$ nanobars in the degradation of MB. This may be mainly due to the active sites generated by the *in-situ* formation of Ag nanoparticles on α-$AgVO_3$ nanorods [33]. It has also been demonstrated that an ordered

mesoporous structure is highly desirable for effective photocatalysis [47]. The HRTEM image of the nanorod clearly shows the crystalline lattice decorated with Ag particles. Also the α-$AgVO_3$ nanorods have higher pore volume compared to $BiVO_4$ nanobars. Hence the methylene blue can easily diffuse in to large pores and reach the active sites effectively. The surface charge recombination hinders the activity of a heterogeneous photocatalyst [48]. Reduction of the electron-hole combination rate enhances the photoactivity. Another factor which enhances the photocatalytic activity is the crystallinity of the photocatalyst. In general, the high the crystalline nature, the high is the photocatalytic activity, because recombination between photogenerated electrons and holes is suppressed in highly crystalline photocatalysts [38]. From the XRD studies, it is clear that the peaks in α-$AgVO_3$ nanorods are more sharp than that of $BiVO_4$ nanobars and hence α-$AgVO_3$ nanorods are more crystalline than $BiVO_4$ nanobars. The higher degree of crystallization of the sample decreased the number of grain boundaries, which serve as recombination centres between photo-generated electrons and holes. Therefore a decrease in grain boundaries results in an increase in the photocatalytic activity.

The high degradation efficiency of monoclinic α-$AgVO_3$ is also attributed to the characteristic absorption band in the visible light region [39]. The silver 4d orbitals and the oxygen 2p orbitals were involved in the formation of the valence band resulting in the reduction of the band gap, due to a metal-to-metal charger transfer (MMCT) between the d^{10} Ag^{+} and d^{0} V^{5+} electron configurations [49]. The vanadium 3d orbitals in the conduction band are more positive than the reduction potential of MB. The Ag^{+} ion in the crystal lattice of α-$AgVO_3$ nanorods make the valence band more

negative [50].Hence the α-$AgVO_3$ nanorods exhibit higher photocatalytic activities compared to $BiVO_4$ nanobars.

The development of such photocatalysts may be considered a breakthrough in large-scale utilization of heterogeneous photocatalysis via visible light to address water contamination and environmental pollution.

4.6. Conclusion

We have developed a facile and simple room temperature aqueous precipitation route for the synthesis of monoclinic α-$AgVO_3$ nanorods and monoclinic $BiVO_4$ nanobars with high aspect ratio by controlling the reaction kinetics. No capping agents or surfactants are used for the synthesis. This facile method is very economic, highly reproducible, fast and worth exploring for the synthesis of one-dimensional nano structures. Possible growth mechanisms of the nanocrystals are explained by the oriented attachment of flocs through an anisotropic growth. The TEM images show that Ag nanoparticles are formed *in-situ* on monoclinic α-$AgVO_3$ nanorods. Using diffuse reflectance spectral analysis the band gap of monoclinic α-$AgVO_3$ nanorods and monoclinic $BiVO_4$ nanobars are calculated.

A comparative study of the photocatalytic activity of the synthesized nanophased vanadates on the degradation of methylene blue (MB) solution under visible light irradiation is also investigated. It is found that about 45% of the MB is degraded within 30 minutes by monoclinic α-$AgVO_3$ nanorods on visible light irradiation. At this time the degradation efficiency of monoclinic $BiVO_4$ nanobars is found to be only 10% and the self degradation efficiency of MB is 0%. But after 30 minutes, the efficiency of monoclinic $BiVO_4$ nanobars increases.

The photocatalytic evaluation revealed that the monoclinic α-$AgVO_3$ nanorods exhibit a higher photocatalytic performance than monoclinic $BiVO_4$ nanobars. The α-$AgVO_3$ nanorods have high pore volume compared to $BiVO_4$ nanobars. The methylene blue can easily diffuse in to large pores and reach the active sites effectively. The Ag nanoparticles attached on the surface of monoclinic α-$AgVO_3$ nanorods also serve as active sites. Hence it is a good candidate for visible light driven photocatalyst.

In the countries where ample amount of sunlight is available, photo catalysis involving sunlight will be economical and preferable. Photocatalytic degradation of organic contaminants using solar irradiation could be highly economical compared with the processes using artificial UV irradiation, which required substantial electrical power input. The efficient utilization of the visible portion of the solar spectrum is essential in both solar hydrogen generation and the photocatalytic decomposition of organic pollutants. This study provides a facile route, using common and inexpensive reagents and equipments, which might be suitable for the large scale synthesis of highly active visible-light driven photocatalysts.

4.7. References

1. P.K. Ghosh, U.N. Maiti, K.K. Chattopadhyay, *Mater. Lett.*, 60 (2006) 2881
2. X. He, M. Cao, *Nanotechnology*, 17 (2006) 3139
3. Q. Lu, F. Gao, S. Komarneni, *Nanotechnology*, 17 (2006) 2574
4. G. Cao, *Nanostructures & Nanomaterials, Synthesis, Properties & Applications*, Imperial College Press, London, (2004) 7- 9

5. C. Burda, X. Chen, R. Narayanan, M.A. El-Sayed, *Chem. Rev.*, 105 (2005) 1025
6. T. Ahamad, S. Vaiya, N. Sarkar, S. Ghosh, A.K. Ganguli, *Nanotechnology*, 17 (2006) 1236
7. Y. Chen, C. Liu, F. Li, H.M. Cheng, *J. Alloys Compd.*, 397 (2005) 282
8. H. Chen, Y. Nie, L. Wang, J. Zhang, F. Dong, Q. Dai, H. Lu, S. Gao, D. Li, S. Kan, G. Zou, *Nanotechnology*, 17 (2006) 3144
9. G. Du, G.V. Tandeloo, *Nanotechnology*, 16 (2005) 595
10. U.K. Gautam, M. Nath, C.N.R. Rao, *J. Mater. Chem.*, 13 (2003) 2845
11. C.M. Janet, R.P. Viswanath, *Nanotechnology*, 17 (2006) 5271
12. U.A. Joshi, J.S. Lee, *Inorg. Chem.*, 46 (2007) 3176
13. S. Kwan, F. Kim, J. Akana, P. Yang, *Chem. Commun.*, (2001) 447
14. Y. Zhang, Y. Liu, S. Fu, F. Guo, Y. Quan, *Bull. Chem. Soc. Jpn.*, 79(2) (2006) 270
15. X. Zhang, Z. Ai, F. Jia, L. Zhang, X. Fan, Z. Zou, *Mater. Chem. Phys.*, 103 (2007) 162
16. Z. Huang, P.C. Maness, D. Blake, E.J. Wolfrum, S.L. Smolinski, W.A. Jacoby, *J. Photochem. Photobiol. A*, 130 (2000) 163
17. D.S. Bhatkhande, V.G. Pangarkar, A.ACM. Beenackers, *J. Chem. Technol.*, 77 (2002) 102
18. T. Bak, J. Nowotny, M. Rekas, C.C. Sorrell, *Int. J. Hydrogen Energy*, 27 (2002) 1022
19. R. Asahi, T. Morikawa, T. Ohwaki, K. Aoki, Y. Taga, *Science*, 293 (2001) 269
20. C. Hu, Y. Lan, J. Qu, X. Hu, A. Wang, *J. Phys. Chem., B*, 110 (2006) 4066

21. K. Sayama, A. Nomura, Z. G. Zou, R.Abe, Y. Abe, H. Arakawa, *Chem. Commun.*, (2003) 2908
22. K. Sayama, A. Nomura, T. Arai, T. Sugita, R. Abe, M. Yanagida, T. Oi, Y.Iwasaki, Y. Abe, H. Sugihara, *J. Phys. Chem.* B, 110 (2006) 11352
23. T. Radhika, S. Sugunan, *J. Mol. Catal. A: Chem.*, 250 (2006) 169
24. J.M. Vohs, T. Feng, G.S. Wong, *Catal. Today*, 85 (2003) 303
25. R. Konta, H. Kato, H. Kobayashi, A. Kudo, *Phys. Chem. Chem. Phys.*, 5 (2003) 3061
26. S. Sun, W. Wang, L. Zhou, H. Xu *Ind. Eng. Chem. Res.*, 48 (2009) 1735
27. K. Sayama, A. Nomura, T. Arai, T. Sugita, R. Abe, M. Yanagida, T. Oi, Y. Iwasaki, Y. Abe, H. Sugihara, J. *Phys. Chem. B*, 110 (2006) 11352
28. L. Zhou, W.Z. Wang, S.W. Liu, L.S. Zang, H.L. Xu, W. Zhu, *J. Mol. Catal. A*, 252 (2006) 120
29. P. Kubelka, F. Munk, *Tech. Z. Phys.*,12 (1931) 593
30. JCPDS card No. 89-4396
31. JCPDS card No. 75-1866
32. S. Sharma, M. Panthofer, M. Jansen, A. Ramanan, *Mater. Chem. Phys.*, 91 (2005) 257
33. G. Li, K. Chao, C. Ye, H. Peng, *Mater. Lett.*, 62 (2008) 735
34. R .Ferrando,. R. Baletto, *Rev. Mod. Phys.*, 77 (2005) 371
35. P. M Ajayan, L. D. Marks, *Phys. Rev. Lett.*, 60 (1998) 585
36. D.H. Everett, *Basic Principles of Colloid Science,* Royal Society of Chemistry, London, (1988) 127
37. X. Peng, L. Manna, W. Yang, J. Wickham, E. Scher, A. Kadavanich, A.P. Alivisatos, *Nature,* 404 (2000) 59
38. C. Zhang, Y. Zhu, *Chem. Mater.*, 17 (2005) 3537

39. R. Konta, H. Kato, H. Kobayashi, A. Kudo, *Phys. Chem. Chem. Phys.*, 5 (2003) 3061
40. A. Kudo, K. Omori, H. Kato, *J. Am. Chem. Soc.*, 121 (1999) 11459
41. M.A. Butler, *J. Appl. Phys.*, 48 (1977) 1914
42. L. Zhou, W.Z. Wang, S.W. Liu, L.S. Zang, H.L. Xu, W. Zhu, *J. Mol. Catal. A,* 252 (2006) 120
43. S. Sun, W. Wang, L. Zhou, H. Xu, *Ind. Eng. Chem. Res.,* 48(2009) 1735
44. J.C. Yu, J.G. Yu, W.K. Ho, Z.T. Jiang, L.Z. Zhang, *Chem. Mater.*, 14(9) (2002) 3808
45. J.G. Yu, J.C. Yu, W.K. Ho, Z.T. Jiang, *New J. Chem.*, 26 (2002) 607
46. S. Chen, S. Zhang, W. Liu, W. Zhao, *J. Hazardous Mater.,* 155 (2008) 320
47. G. Li, D. Zhang, J. C. Yu, *Chem. Mater.*, 20 ((2008) 3983
48. R. Ullah, J. Dutta, *J. Hazardous Materials,* 156 (2008) 194
49. H. Lin, P.A. Maggard, *Inorg. Chem.*, 47 (2008) 8044
50. H. Kato, H. Kobayashi, A. Kudo, *J. Phys. Chem. B,* 106 (2002) 12441